



# The MOSDEF Survey: [S III] as a New Probe of Evolving Interstellar Medium Conditions\*

Ryan L. Sanders<sup>1</sup> , Tucker Jones<sup>1</sup> , Alice E. Shapley<sup>2</sup> , Naveen A. Reddy<sup>3,11</sup> , Mariska Kriek<sup>4</sup> , Alison L. Coil<sup>5</sup> , Brian Siana<sup>3</sup> , Bahram Mobasher<sup>3</sup>, Irene Shivaei<sup>6,12</sup> , Sedona H. Price<sup>7</sup> , William R. Freeman<sup>3</sup> , Mojegan Azadi<sup>8</sup> , Gene C. K. Leung<sup>5</sup> , Tara Fetherolf<sup>3</sup>, Tom O. Zick<sup>4</sup>, Laura de Groot<sup>9</sup> , Guillermo Barro<sup>10</sup> , and Francesca M. Fornasini<sup>8</sup>

<sup>1</sup> Department of Physics, University of California, Davis, One Shields Avenue, Davis, CA 95616, USA; [rlsand@ucdavis.edu](mailto:rlsand@ucdavis.edu)

<sup>2</sup> Department of Physics & Astronomy, University of California, Los Angeles, 430 Portola Plaza, Los Angeles, CA 90095, USA

<sup>3</sup> Department of Physics & Astronomy, University of California, Riverside, 900 University Avenue, Riverside, CA 92521, USA

<sup>4</sup> Astronomy Department, University of California, Berkeley, CA 94720, USA

<sup>5</sup> Center for Astrophysics and Space Sciences, University of California, San Diego, 9500 Gilman Drive, La Jolla, CA 92093-0424, USA

<sup>6</sup> Department of Astronomy/Steward Observatory, 933 North Cherry Avenue, Room N204, Tucson, AZ 85721-0065, USA

<sup>7</sup> Max-Planck-Institut für extraterrestrische Physik, Postfach 1312, Garching, D-85741, Germany

<sup>8</sup> Harvard-Smithsonian Center for Astrophysics, 60 Garden Street, Cambridge, MA 02138, USA

<sup>9</sup> Department of Physics, The College of Wooster, 1189 Beall Avenue, Wooster, OH 44691, USA

<sup>10</sup> Department of Physics, University of the Pacific, 3601 Pacific Avenue, Stockton, CA 95211, USA

Received 2019 October 30; revised 2019 November 25; accepted 2019 November 29; published 2019 December 31

## Abstract

We present measurements of [S III] $\lambda\lambda$ 9069,9531 for a sample of  $z \sim 1.5$  star-forming galaxies, the first representative sample with measurements of these lines at  $z \gtrsim 0.1$ . We employ the line ratio  $S_{32} \equiv [\text{S III}]\lambda\lambda 9069,9531 / [\text{S II}]\lambda\lambda 6716,6731$  as a novel probe of evolving interstellar medium (ISM) conditions. Since this ratio includes the low-ionization line [S II], it is crucial that the effects of diffuse ionized gas (DIG) on emission-line ratios be accounted for in  $z \sim 0$  galaxy spectra, or else that comparisons be made to samples of local H II regions in which DIG emission is not present. We find that  $S_{32}$  decreases with increasing stellar mass at both  $z \sim 1.5$  and  $z \sim 0$ , but with a shallow slope suggesting  $S_{32}$  has a weak dependence on metallicity, in contrast with [O III]/[O II] that displays a strong metallicity dependence. As a result,  $S_{32}$  only mildly evolves with redshift at fixed stellar mass. The  $z \sim 1.5$  sample is systematically offset toward lower  $S_{32}$  and higher [S II]/H $\alpha$  at fixed [O III]/H $\beta$  relative to  $z = 0$  H II regions. We find that such trends can be explained by a scenario in which the ionizing spectrum is harder at fixed O/H with increasing redshift, but are inconsistent with an increase in ionization parameter at fixed O/H. This analysis demonstrates the advantages of expanding beyond the strongest rest-optical lines for evolutionary studies, and the particular utility of [S III] for characterizing evolving ISM conditions and stellar compositions. These measurements provide a basis for estimating [S III] line strengths for high-redshift galaxies, a line that the *James Webb Space Telescope* will measure out to  $z \sim 5.5$ .

*Unified Astronomy Thesaurus concepts:* [Galaxy evolution \(594\)](#); [High-redshift galaxies \(734\)](#); [Interstellar medium \(847\)](#)

## 1. Introduction

The rest-optical emission lines of star-forming galaxies provide valuable insight into the physical properties of the ionized gas in H II regions. Diagnostics of nebular metallicity (O/H), ionization parameter ( $U$ ), and electron density have been calibrated at  $z \sim 0$ . An additional important consideration is the shape of the stellar spectrum ionizing the gas, primarily determined by the Fe/H of massive stars. Due to tight relations between these properties, H II regions and local star-forming galaxies follow excitation sequences in emission-line ratio diagrams, including the [O III]/H $\beta$  versus [N II]/H $\alpha$  and [S II]/H $\alpha$  Baldwin, Phillips & Terlevich (BPT) diagrams (Baldwin et al. 1981; Veilleux & Osterbrock 1987). Recent large near-infrared spectroscopic surveys at  $z \sim 2$  have demonstrated that high-redshift star-forming galaxies follow a sequence that is systematically offset from the  $z \sim 0$  sequence

in the [N II] BPT diagram (e.g., Steidel et al. 2014; Sanders et al. 2016; Kashino et al. 2019; Shapley et al. 2019). This shift in the excitation sequence implies that the ionized interstellar medium (ISM) conditions are changing with redshift, and in particular that at least some of the relations between O/H,  $U$ , and stellar Fe/H evolve.

Determining which parameters evolve at fixed O/H and by how much has proven difficult. Such work often relies on photoionization models to understand how each line ratio changes when the relevant ISM conditions are varied (e.g., Kewley et al. 2013; Steidel et al. 2014; Sanders et al. 2016; Strom et al. 2017). A particular challenge lies in characterizing the ionization parameter and hardness of the ionizing spectrum, as neither is simply tied to an observable and the two are highly degenerate when O/H is unknown. Useful constraints cannot be obtained when only a few rest-optical lines are available (the case for most high-redshift galaxies), and degeneracies and large uncertainties remain even when five to six strong rest-optical lines are available (Strom et al. 2018). Only one “pure” ionization parameter diagnostic is available among the strongest optical lines ([O III]/[O II]) and it is strongly affected by dust reddening. A better understanding of evolving ISM conditions can be obtained by introducing additional line ratios

\* Based on data obtained at the W.M. Keck Observatory, which is operated as a scientific partnership among the California Institute of Technology, the University of California, and NASA, and was made possible by the generous financial support of the W.M. Keck Foundation.

<sup>11</sup> Alfred P. Sloan Fellow.

<sup>12</sup> Hubble Fellow.

as constraints that move beyond the strongest optical lines ([O II], H $\beta$ , [O III], H $\alpha$ , [N II], [S II]), most preferably an additional ionization parameter diagnostic ratio of a single element that is relatively unaffected by reddening.

In this Letter we present the first measurements of [S III]  $\lambda\lambda 9069,9531$  for a representative sample at  $z > 1$  and explore the utility of the  $S_{32} \equiv [\text{S III}]\lambda\lambda 9069,9531/[\text{S II}]\lambda\lambda 6716,6731$  ratio for constraining evolving ISM conditions. This analysis uses observations of star-forming galaxies at  $z \sim 1.5$  from the MOSFIRE Deep Evolution Field survey (MOSDEF; Kriek et al. 2015) in combination with galaxy and H II region samples from the local universe. In Section 2, we present the [S III] detections for individual high-redshift galaxies and composite spectra, and describe the low-redshift comparison samples. We investigate the evolution of  $S_{32}$  at fixed stellar mass ( $M_*$ ) in Section 3. Finally, we present excitation sequences of [S III] and [S II] ratios in Section 4 and discuss implications for the evolving physical conditions in H II regions. Emission-line wavelengths are given in air. We assume a  $\Lambda$ CDM cosmology with  $H_0 = 70 \text{ km s}^{-1} \text{ Mpc}^{-1}$ ,  $\Omega_m = 0.3$ , and  $\Omega_\Lambda = 0.7$ .

## 2. Observations, Data, and Samples

### 2.1. The $z \sim 1.5$ MOSDEF Sample

We draw a sample of high-redshift galaxies with [S III] measurements from the MOSDEF survey, a four-year program that obtained rest-frame optical spectra of  $\sim 1500$  galaxies at  $1.37 \leq z \leq 3.80$ . A detailed description of the survey and data reduction can be found in Kriek et al. (2015). The MOSDEF flux calibration is robust between filters, such that ratios of lines from different filters (e.g., [S III]/[S II]) are biased less than 0.05 dex on average with a scatter of 0.07 dex (Kriek et al. 2015). We utilize emission-line measurements, stellar masses, reddening estimates, and star formation rates (SFRs) from the MOSDEF catalogs. Stellar masses and continuum reddening are estimated from emission-line corrected photometry via spectral energy distribution (SED) fitting using the code FAST (Kriek et al. 2009), assuming constant star formation histories, solar metallicity, a Chabrier (2003) initial mass function (IMF), and the Calzetti et al. (2000) attenuation curve. Nebular reddening is estimated using the H $\alpha$ /H $\beta$  ratio when both lines are detected at signal-to-noise ratio (S/N)  $\geq 3$ , assuming an intrinsic ratio of 2.86 and the Cardelli et al. (1989) extinction curve. When H $\beta$  is not detected, we infer  $E(B-V)_{\text{gas}}$  from continuum reddening under the assumption that  $E(B-V)_{\text{gas}} \approx E(B-V)_{\text{stars}}$ , as found to be true on average at  $z \sim 2$  (Kashino et al. 2013; Reddy et al. 2015). SFRs are derived from reddening-corrected H $\alpha$  luminosity using the Hao et al. (2011) calibration converted to a Chabrier (2003) IMF.

Galaxies were targeted in three redshift bins:  $1.37 \leq z \leq 1.70$ ,  $2.09 \leq z \leq 2.61$ , and  $2.95 \leq z \leq 3.80$ . Masks in each redshift bin were observed in multiple near-infrared filters in which the [O II], H $\beta$ , [O III], H $\alpha$ , [N II], and [S II] emission lines fall. Accordingly,  $z \sim 1.5$  masks were observed in  $Y$ ,  $J$ , and  $H$  bands;  $z \sim 2.3$  masks in  $J$ ,  $H$ , and  $K$ ; and  $z \sim 3.4$  masks in  $H$  and  $K$  only. [S III] lies significantly redward of [S II], falling in the  $K$ -band at  $z \sim 1.5$  and redshifted out of the bands of atmospheric transmission at  $z > 2$ . Thus, most MOSDEF  $z \sim 1.5$  targets do not have [S III] measurements because observations in the  $K$ -band are lacking. However, there are 49 MOSDEF star-forming galaxies at

$1.25 \leq z \leq 1.65$  with  $K$ -band observations because they were either filler targets (26) or serendipitous detections (23) on  $z > 2$  masks. At least one [S III] line is detected at S/N  $\geq 3$  for 10 individual galaxies in this sample, with both lines detected in four. The spectra of these 10 objects are presented in Figure 1. In addition to individual detections and limits, we stacked spectra to obtain average [S III] measurements for the sample and include non-detections. We created multiple composite spectra following the procedure of Sanders et al. (2018), requiring H $\alpha$  S/N  $\geq 3$  as well as the additional criteria described in Table 1 for each. In brief, individual spectra were converted to luminosity density, normalized by H $\alpha$  luminosity, shifted onto a common rest-wavelength grid, and median stacked without weighting. This process ensures that high-SFR galaxies do not dominate the composite line ratios. The *Stack1* composite spectrum with coverage of both [S III] lines is displayed in the top row of Figure 1.

### 2.2. The $z \sim 0$ Comparison Samples

Most large spectroscopic  $z \sim 0$  galaxy surveys (e.g., the Sloan Digital Sky Survey (SDSS); York et al. 2000) do not have coverage extending to  $\approx 1 \mu\text{m}$ , required for [S III] measurements. To obtain a  $z \sim 0$  galaxy comparison sample, we use data from the Mapping Nearby Galaxies at APO (MaNGA) integral field spectroscopic survey (Bundy et al. 2015), with coverage out to  $1.04 \mu\text{m}$ . We employ the MaNGA PIPE3D catalog of emission-line measurements (Sánchez et al. 2016, 2018), which includes spatially resolved line fluxes and uncertainties as well as tabulated [O III]/H $\beta$  and [N II]/H $\alpha$  ratios in the central  $2''5$  of each galaxy. We select star-forming galaxies using the central line ratios based on the demarcation of Kauffmann et al. (2003) and restrict the redshift to  $z < 0.08$  to ensure that [S III] $\lambda 9531$  falls in the bandpass, yielding a sample of 1150 star-forming galaxies with a median redshift of  $z_{\text{med}} = 0.026$ . The MaNGA sample has a lower median redshift than typical SDSS star-forming galaxy samples with  $z_{\text{med}} \approx 0.07\text{--}0.10$  (e.g., Tremonti et al. 2004; Andrews & Martini 2013). To obtain integrated galaxy spectra similar to SDSS fiber spectra, we sum the MaNGA line fluxes within the central  $10'' \times 10''$  corresponding to a 5 kpc width at  $z = 0.026$ , equivalent to the physical diameter covered by a  $3''$  SDSS fiber at  $z = 0.085$ .

We also compare to  $z = 0$  H II regions in three spiral galaxies from the Chemical Abundances Of Spirals (CHAOS) survey (NGC 628, Berg et al. 2015; NGC 5194, Croxall et al. 2015; NGC 5457, Croxall et al. 2016). This sample comprises 213 individual H II regions with detections of both [S III] lines, spanning a wide range of metallicity ( $0.1\text{--}2.0 Z_\odot$ ).

### 2.3. The [S III] $\lambda 9531/\lambda 9069$ Ratio

Not all of our targets are detected in both [S III] lines. Accordingly, we need to convert the line flux of one line to the total doublet flux. This approach is possible because the ratio [S III] $\lambda 9531/\lambda 9069$  is fixed to a value of  $\approx 2.5$  according to the transition probabilities (Osterbrock & Ferland 2006; Tayal et al. 2019). We show the [S III] $\lambda 9531/\lambda 9069$  ratios for individual  $z \sim 1.5$  galaxies, the *Stack1*  $z \sim 1.5$  composite, and the  $z \sim 0$  comparison samples in Figure 2. We find that *Stack1* and three out of four  $z \sim 1.5$  galaxies are consistent with the theoretically expected ratio within  $1\sigma$ . The single offset  $z \sim 1.5$  galaxy displays possible skyline contamination on the red wing

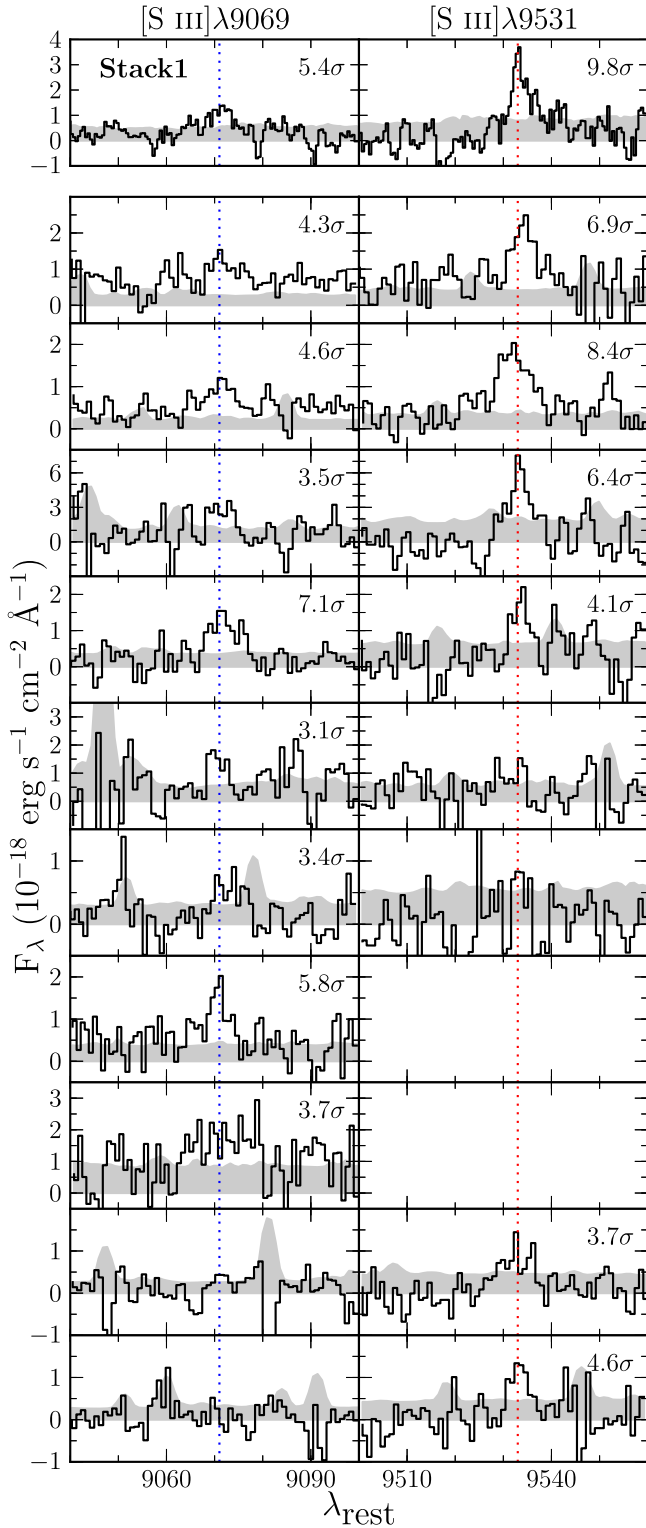


**Figure 1.** Science spectra (black) and error spectra (gray) displaying detections of [S III] $\lambda$ 9069 (left column) and [S III] $\lambda$ 9531 (right column) at  $z \sim 1.5$  from the MOSDEF survey. All rows except the top show spectra of individual star-forming galaxies. The top row presents the *Stack1* composite spectrum with flux arbitrarily normalized. The significance of the emission-line detection is given in the top-right corner of panels when  $S/N \geq 3$ .

of [S III] $\lambda$ 9531 (Figure 1, fifth row). The  $z = 0$  CHAOS H II regions also match the expected value on average. The median ratio of the  $z \sim 0$  MaNGA sample is 2.12, significantly lower than the expected value. This offset may indicate that Paschen-

**Table 1**  
Description of the  $z \sim 1.5$  [S III] Composite Spectra

Name	Selection Criteria	$N_{\text{gal}}^a$	$\langle \log(\frac{M_*}{M_\odot}) \rangle^b$
<i>Stack1</i>	[S III] $\lambda$ 9069 and [S III] $\lambda$ 9531 coverage	28	9.78
<i>Stack2</i>	[S III] $\lambda$ 9069 coverage and two bins in $M_*$	35, 11 <sup>c</sup>	9.54, 10.21 <sup>c</sup>
<i>Stack3</i>	[S III] $\lambda$ 9069, [O III] $\lambda$ 5007, and H $\beta$ coverage	29	9.85

**Notes.**

<sup>a</sup> The number of galaxies included in each composite.

<sup>b</sup> The median stellar mass of the galaxies in each composite.

<sup>c</sup> The low-mass bin is listed first, followed by the high-mass bin. The two mass bins, split at  $10^{9.94} M_\odot$ , were populated such that equivalent S/N is obtained on [S III] $\lambda$ 9069 in both composite spectra.

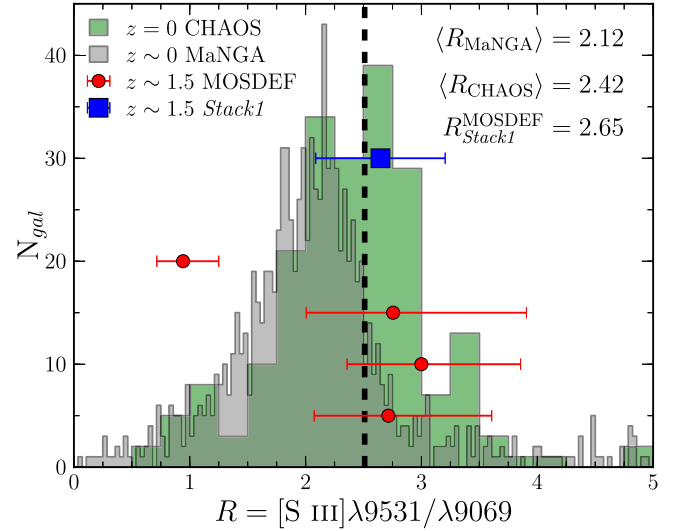


**Figure 2.** Histogram of [S III] $\lambda$ 9531/ $\lambda$ 9069 for  $z = 0$  H II regions from the CHAOS survey (green) and  $z \sim 0$  star-forming galaxies from the MaNGA survey (gray). Red points show the four  $z \sim 1.5$  MOSDEF star-forming galaxies with  $S/N \geq 3$  detections of both lines, placed at arbitrary  $y$ -axis positions. The blue square presents the ratio measured from the *Stack1* composite spectrum. The *Stack1* ratio and median values for the  $z \sim 0$  samples are given in the top-right corner. The dashed vertical line shows the theoretically predicted value of 2.5.

$\epsilon$  absorption at 9546 Å has not been fully accounted for. To avoid biasing the total [S III] fluxes low, we only use [S III] $\lambda$ 9069 for the MaNGA sample. For all samples and composites, we infer the total [S III] $\lambda$ 9069,9531 flux assuming that [S III] $\lambda$ 9531/ $\lambda$ 9069 = 2.5 when only one [S III] line is detected.

### 3. $S_{32}$ and Global Galaxy Properties

We now investigate the evolution of the emission-line ratio  $S_{32} \equiv [\text{S III}]\lambda\lambda 9069,9531 / [\text{S II}]\lambda\lambda 6716,6731$ . We begin by characterizing the global galaxy properties of the  $z \sim 1.5$  [S III] sample. In the top panel of Figure 3, we show SFR versus  $M_*$  for the  $z \sim 1.5$  MOSDEF and  $z \sim 0$  MaNGA samples. The  $z \sim 1.5$  galaxies with [S III] detections (red) and those with [S III] coverage but no detections (pink) fall on the mean  $z \sim 1.5$   $M_*$ -SFR relation described by the full MOSDEF  $z \sim 1.5$  star-forming sample (cyan). The [S III] subset has a lower average  $M_*$  ( $\sim 10^{9.7} M_\odot$ ) than the full MOSDEF sample ( $\sim 10^{10.0} M_\odot$ ), but is not significantly biased in SFR at fixed

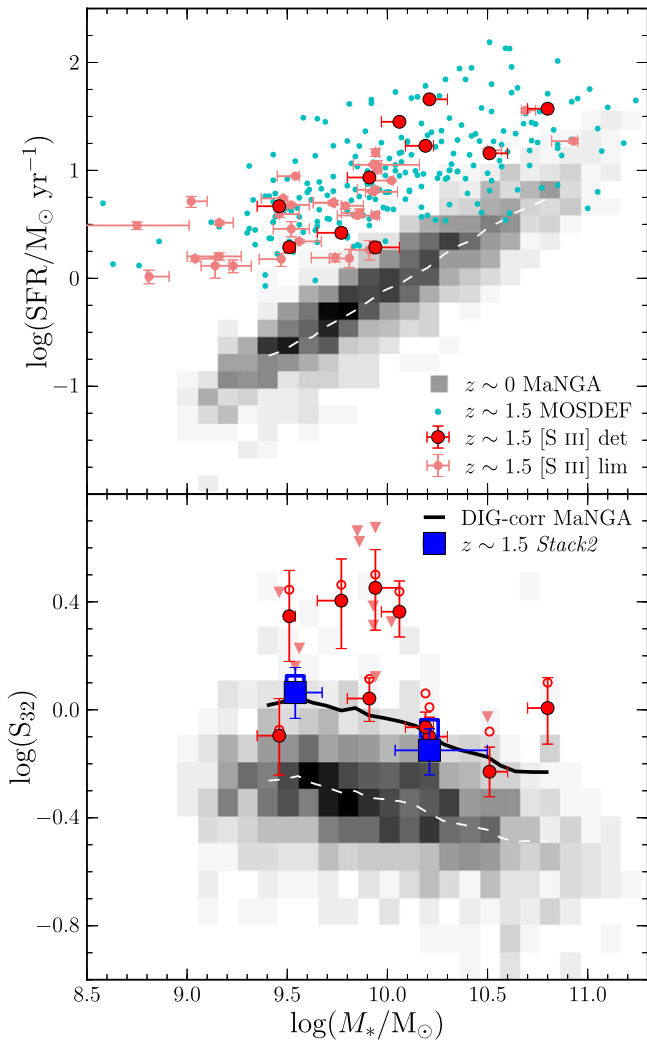


**Figure 3.** SFR (top) and  $S_{32} \equiv [\text{S III}]/[\text{S II}]$  (bottom) vs. stellar mass. Filled red points show individual  $z \sim 1.5$  star-forming galaxies with detections of at least one [S III] line. In the top panel, pink circles denote  $z \sim 1.5$  galaxies with wavelength coverage of [S III] but without detections, while pink triangles show upper limits on  $S_{32}$  in the lower panel. Cyan points in the top panel present the full  $z \sim 1.5$  MOSDEF star-forming sample with  $\text{H}\alpha$   $\text{S/N} \geq 3$ . The gray two-dimensional histogram shows the distribution of the  $z \sim 0$  MaNGA sample, with running medians displayed as white dashed lines. The black solid line in the bottom panel shows the MaNGA median after correcting [S II] emission for DIG contamination. Blue filled squares in the bottom panel present the low- and high-mass composites of *Stack2*. Open blue and red points denote  $S_{32}$  values prior to reddening correction.

$M_*$ . Both individual [S III]-detected galaxies and stacks including non-detections are representative of the typical  $z \sim 1.5$  star-forming population.

The bottom panel of Figure 3 displays  $S_{32}$  versus  $M_*$ . Individual  $z \sim 1.5$  galaxies span a wide range of  $S_{32}$ , with the highest  $S_{32}$  values occurring in the low-mass half of the sample. Blue squares show stacks of  $z \sim 1.5$  spectra in two  $M_*$  bins (*Stack2*). At fixed  $M_*$ , [S III]-detected galaxies lie at higher  $S_{32}$  than the stacks due to preferential detection of high-excitation galaxies with stronger [S III]. We find that  $S_{32}$  decreases with increasing  $M_*$  for both the  $z \sim 1.5$  and  $z \sim 0$  samples, indicative of lower ionization parameter at higher  $M_*$  and higher metallicity. The anticorrelation between  $S_{32}$  and  $M_*$  displays a similar slope at  $z \sim 1.5$  and  $z \sim 0$ , but the  $z \sim 1.5$  galaxies are offset 0.25 dex higher in  $S_{32}$  at fixed  $M_*$ .

It has been shown that [S II] is significantly enhanced in  $z \sim 0$  integrated galaxy spectra due to diffuse ionized gas (DIG) emission, which is expected to be negligible at high redshifts (Zhang et al. 2017; Sanders et al. 2017; Shapley et al. 2019). DIG contamination thus biases redshift evolution comparisons. We correct for DIG contamination of [S II] in the MaNGA line ratios according to the prescription of Sanders et al. (2017), removing the DIG contribution and yielding the contribution from H II regions only. The effect of DIG on galaxy-integrated [S III] emission has not yet been investigated. However, DIG contribution to [S III] is not expected to be strong because DIG primarily enhances low-ionization species. After correcting the MaNGA sample for DIG contamination of [S II], the relation between  $S_{32}$  and  $M_*$  appears to be nearly the same at  $z \sim 0$  (black line) and  $z \sim 1.5$  (blue squares).

Many strong-line ratios (e.g., [O III]/ $\text{H}\beta$ , [O III]/[O II]) display significant evolution toward higher excitation at fixed  $M_*$  even after accounting for  $z \sim 0$  DIG (Sanders et al. 2016, 2018), thought to primarily reflect evolution toward lower metallicity at fixed  $M_*$  with increasing redshift. We now examine whether the observed lack of significant  $S_{32}$  evolution after DIG correction is consistent with this picture. Mass-metallicity relation studies at both  $z \sim 0$  and  $z \sim 1.5$  find  $\Delta \log(\text{O}/\text{H}) \sim 0.6$  dex over a decade in  $M_*$  at fixed redshift (Zahid et al. 2014; Kashino et al. 2017), while Figure 3 shows  $S_{32}$  changes by  $\sim 0.2$  dex over the same mass interval. Accordingly,  $S_{32}$  has a very weak dependence on metallicity ( $\Delta \log(S_{32}) \approx 0.33 \times \Delta \log(\text{O}/\text{H})$ ). Indeed,  $S_{32}$  displays a much weaker dependence on metallicity than [O III]/[O II] in photoionization models (Kewley et al. 2019). From  $z \sim 0$  to  $z \sim 1.5$ , O/H decreases by  $\sim 0.2$  dex at fixed  $M_*$  corresponding to an expected increase in  $S_{32}$  of only  $\sim 0.07$  dex. This difference is smaller than the *Stack2* error bars. We thus find that the lack of significant  $S_{32}$  evolution at fixed  $M_*$  after DIG correction is fully consistent with the evolution of the mass-metallicity relation.

#### 4. $S_{32}$ and Evolving ISM Conditions

We now turn to the evolution of excitation sequences in emission-line ratio diagrams and the changing the physical conditions of ionized gas in H II regions with redshift. In Figure 4, we show [O III]/ $\text{H}\beta$  versus [S II]/ $\text{H}\alpha$  (left column) and  $S_{32}$  (right column). The top row displays empirical data sets. In the top-left panel, the  $z \sim 1.5$  sample displays larger [S II]/ $\text{H}\alpha$  at fixed [O III]/ $\text{H}\beta$  than  $z = 0$  H II regions on average, but is offset toward lower [S II]/ $\text{H}\alpha$  compared to the  $z \sim 0$  MaNGA galaxies. The severe offset between the H II regions and  $z \sim 0$  galaxies demonstrates the strong influence of DIG emission on [S II] (Sanders et al. 2017; Shapley et al. 2019). Correcting [S II] and [O III] emission for DIG contamination following Sanders et al. (2017) yields the black line that closely matches the median sequence of the H II regions. In the top-right panel, the  $z \sim 1.5$  sample lies on the sequence described by  $z \sim 0$  MaNGA galaxies, but is offset from the  $z = 0$  H II region sequence toward lower  $S_{32}$  at fixed [O III]/ $\text{H}\beta$ . Once again, the influence of DIG emission biases the comparison to low-redshift galaxies.

To interpret these offsets, we employ the set of photoionization models described in Sanders et al. (2020) to identify the qualitative shift in these line ratios when varying H II region physical conditions. These models were run using Cloudy (Ferland et al. 2017) with BPASS v2.2.1 binary models

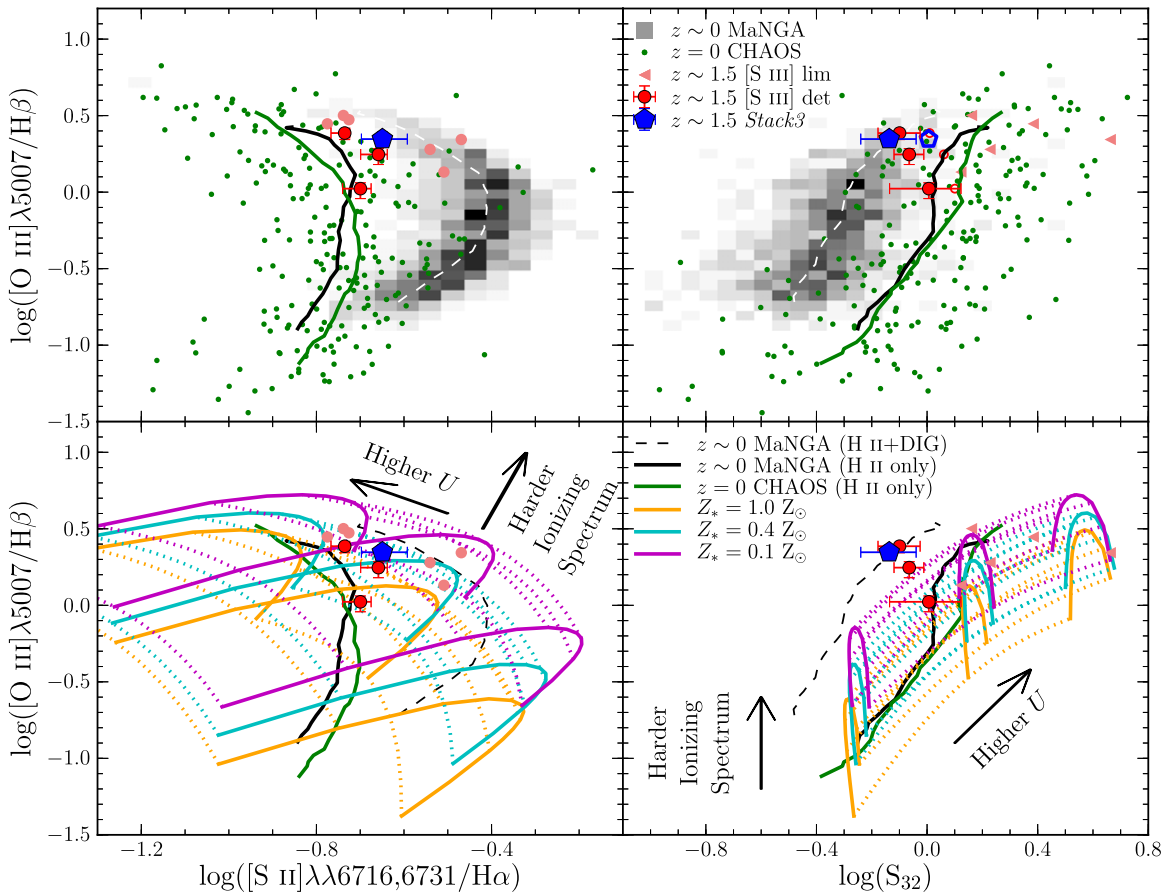


**Figure 4.** Emission-line ratio diagrams of  $[\text{O III}]\lambda 5007/\text{H}\beta$  vs.  $[\text{S II}]\lambda\lambda 6716,6731/\text{H}\alpha$  (left column) and  $S_{32} \equiv [\text{S III}]/[\text{S II}]$  (right column) with observations in the top panels and theoretical photoionization model grids in the bottom panels. In the top panels, green points show individual  $z = 0$  H II regions from the CHAOS survey. The blue filled pentagon presents the line ratios of the  $z \sim 1.5$  *Stack3* composite, while the open pentagon shows the values without reddening correction. All other points are as in Figure 3. The green and white dashed lines display the running median as a function of  $[\text{O III}]\lambda 5007/\text{H}\beta$  for the CHAOS and MaNGA samples, respectively. The solid black line shows the MaNGA median after correcting  $[\text{S II}]$  and  $[\text{O III}]$  emission for DIG contamination. In the bottom panels, photoionization models grids are displayed, color-coded by stellar metallicity that is a proxy for the hardness of the ionizing spectrum. Lines of constant ionization parameter are solid, while lines of constant metallicity are dotted. Black arrows show the qualitative shift when varying only ionization parameter or the hardness of the ionizing spectrum. The  $z \sim 0$  medians and  $z \sim 1.5$  points from the top panels are included for comparison to the model grids, where the  $z \sim 0$  MaNGA median is now dashed black for visibility. The offset between the  $z \sim 1.5$  sample and the  $z = 0$  H II regions or DIG-corrected MaNGA sample can be reproduced with a harder ionizing spectrum at fixed O/H.

(Stanway & Eldridge 2018) as the input radiation field, where the stellar metallicity ( $Z_* = \text{Fe}/\text{H}$ ) is a proxy for the hardness of the ionizing spectrum. The grids span  $0.05\text{--}1.5 Z_\odot$  in nebular metallicity and  $\log U = -2.5$  to  $-3.5$ , and are color-coded by  $Z_*$ . Lines of constant ionization parameter are solid and lines of constant O/H are dotted. The models adopt an electron density of  $n_e = 250 \text{ cm}^{-3}$ , typical at  $z \sim 2$  (Sanders et al. 2016). Varying  $n_e$  between  $25 \text{ cm}^{-3}$  (typical at  $z \sim 0$ ) and  $250 \text{ cm}^{-3}$  changes  $[\text{O III}]/\text{H}\beta$  and  $[\text{S II}]/\text{H}\alpha$  by  $\lesssim 0.05$  dex and does not change  $S_{32}$ , and does not affect our results.

The grids fail to fully overlap the  $z \sim 1.5$  sample in the bottom-right panel of Figure 4. This failure is likely due to a known problem wherein photoionization models underproduce  $[\text{S II}]$  relative to other lines (see Kewley et al. 2019, and references therein), preventing us from placing quantitative constraints on the gas properties. However, the qualitative direction of line ratio shifts should be robust even in the face of systematic  $[\text{S II}]$  underestimation. We thus proceed by comparing the observed offsets between the  $z \sim 0$  and  $z \sim 1.5$  samples in Figure 4 with the qualitative shifts in model line ratios when varying ionization parameter and the hardness of the ionizing spectrum.

We first consider the scenario where the ionizing spectrum varies with redshift at fixed O/H (i.e., moving between colors at a fixed grid vertex). We find that a harder ionizing spectrum (lower  $Z_*$ ) leads to higher  $[\text{O III}]/\text{H}\beta$  and  $[\text{S II}]/\text{H}\alpha$  while leaving  $S_{32}$  unchanged. As a result, excitation sequences shift toward higher  $[\text{S II}]/\text{H}\alpha$  and lower  $S_{32}$  at fixed  $[\text{O III}]/\text{H}\beta$ , in agreement with the observed offsets between  $z \sim 1.5$  galaxies and  $z = 0$  H II regions or DIG-corrected  $z \sim 0$  MaNGA galaxies. We conclude that the shift in line-ratio excitation sequences between  $z \sim 0$  and  $z \sim 1.5$  is primarily driven by a harder ionizing spectrum at fixed nebular metallicity and does not require significant changes to  $U$  at fixed O/H.

If we instead consider varying the ionization parameter while keeping all other parameters fixed, increasing  $U$  (i.e., moving along dotted lines of a single color) leads to an increase in  $[\text{O III}]/\text{H}\beta$  and  $S_{32}$ , and a decrease in  $[\text{S II}]/\text{H}\alpha$ . The net effect is to shift galaxies toward lower  $[\text{S II}]/\text{H}\alpha$  at fixed  $[\text{O III}]/\text{H}\beta$ , and along the  $[\text{O III}]/\text{H}\beta\text{--}S_{32}$  sequence producing no significant offset in  $S_{32}$  at fixed  $[\text{O III}]/\text{H}\beta$  as lines of constant metallicity run roughly parallel to the full empirical sequences in the lower-right panel. Thus, larger  $U$  at fixed O/H can account for the offset (or lack thereof) between the  $z \sim 1.5$







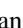





sample and the  $z \sim 0$  MaNGA sample *without DIG correction* (dashed black lines in the lower panels). This conclusion was reached by past studies based on the position of  $z \sim 1.6$  star-forming galaxies in the [S II] BPT diagram relative to a  $z \sim 0$  SDSS sample in which DIG was not accounted for (Kashino et al. 2017, 2019). However, because DIG emission is expected to be negligible in the highly star-forming compact galaxies at high redshifts (Shapley et al. 2019), a fair comparison is either to the H II region sample or to DIG-corrected integrated galaxy spectra, from which the  $z \sim 1.5$  galaxies are offset toward *higher* [S II]/H $\alpha$  and *lower*  $S_{32}$  at fixed [O III]/H $\beta$ . Higher  $U$  at fixed O/H fails to account for these offsets.

Our results thus favor a harder ionizing spectrum at fixed O/H with increasing redshift, in agreement with recent work at  $z \sim 2$  based on deep rest-ultraviolet continuum spectroscopy (Steidel et al. 2016) and electron temperature metallicities (Sanders et al. 2020). However, the measurements utilized in this work can be acquired for many galaxies with a significantly smaller observational investment. Increasing the sample of  $z > 1$  galaxies with [S III] detections thus presents a viable path forward to an understanding of ISM conditions in individual high-redshift galaxies spanning a wide range in  $M_*$ , SFR, and metallicity. Fully leveraging new [S III] observations requires more realistic photoionization models to turn qualitative conclusions into quantitative constraints. Photoionization modeling will be particularly discriminating in cases where both  $S_{32}$  and [O III]/[O II] are available, where the use of two independent ionization parameter diagnostics simultaneously can break degeneracies between the ionizing spectrum and  $U$ . In the next few years, obtaining high-redshift data sets that expand beyond the strongest rest-optical emission lines should be a priority. Such observations are necessary to develop the tools required to interpret the wealth of information from the NIRSpec instrument on the *James Webb Space Telescope*, which will have sufficient sensitivity and wavelength coverage to measure [S III] and numerous other weak lines up to  $z \sim 5.5$ .

We acknowledge support from NSF AAG grants AST-1312780, 1312547, 1312764, and 1313171, grants AR-13907 and GO-15077 provided by NASA through the Space Telescope Science Institute, and grant NNX16AF54G from the NASA ADAP program. We also acknowledge a NASA contract supporting the WFIRST Extragalactic Potential Observations (EXPO) Science Investigation Team (15-WFIRST15-0004), administered by GSFC. We wish to extend special thanks to those of Hawai‘ian ancestry on whose sacred mountain we are privileged to be guests. Without their generous hospitality, the work presented herein would not have been possible.

#### ORCID iDs

Ryan L. Sanders  <https://orcid.org/0000-0003-4792-9119>  
 Tucker Jones  <https://orcid.org/0000-0001-5860-3419>  
 Alice E. Shapley  <https://orcid.org/0000-0003-3509-4855>

Naveen A. Reddy  <https://orcid.org/0000-0001-9687-4973>  
 Mariska Kriek  <https://orcid.org/0000-0002-7613-9872>  
 Alison L. Coil  <https://orcid.org/0000-0002-2583-5894>  
 Brian Siana  <https://orcid.org/0000-0002-4935-9511>  
 Irene Shivaie  <https://orcid.org/0000-0003-4702-7561>  
 Sedona H. Price  <https://orcid.org/0000-0002-0108-4176>  
 William R. Freeman  <https://orcid.org/0000-0003-3559-5270>  
 Mojegan Azadi  <https://orcid.org/0000-0001-6004-9728>  
 Gene C. K. Leung  <https://orcid.org/0000-0002-9393-6507>  
 Laura de Groot  <https://orcid.org/0000-0001-9022-665X>  
 Guillermo Barro  <https://orcid.org/0000-0001-6813-875X>  
 Francesca M. Fornasini  <https://orcid.org/0000-0002-9286-9963>

#### References

- Andrews, B. H., & Martini, P. 2013, *ApJ*, 765, 140  
 Baldwin, J. A., Phillips, M. M., & Terlevich, R. 1981, *PASP*, 93, 5  
 Berg, D. A., Skillman, E. D., Croxall, K. V., et al. 2015, *ApJ*, 806, 16  
 Bundy, K., Bershady, M. A., Law, D. R., et al. 2015, *ApJ*, 798, 7  
 Calzetti, D., Armus, L., Bohlin, R. C., et al. 2000, *ApJ*, 533, 682  
 Cardelli, J. A., Clayton, G. C., & Mathis, J. S. 1989, *ApJ*, 345, 245  
 Chabrier, G. 2003, *PASP*, 115, 763  
 Croxall, K. V., Pogge, R. W., Berg, D. A., Skillman, E. D., & Moustakas, J. 2015, *ApJ*, 808, 42  
 Croxall, K. V., Pogge, R. W., Berg, D. A., Skillman, E. D., & Moustakas, J. 2016, *ApJ*, 830, 4  
 Ferland, G. J., Chatzikos, M., Guzmán, F., et al. 2017, *RMxAA*, 53, 385  
 Hao, C.-N., Kennicutt, R. C., Johnson, B. D., et al. 2011, *ApJ*, 741, 124  
 Kashino, D., Silverman, J. D., Rodighiero, G., et al. 2013, *ApJL*, 777, L8  
 Kashino, D., Silverman, J. D., Sanders, D., et al. 2017, *ApJ*, 835, 88  
 Kashino, D., Silverman, J. D., Sanders, D., et al. 2019, *ApJS*, 241, 10  
 Kauffmann, G., Heckman, T. M., White, S. D. M., et al. 2003, *MNRAS*, 341, 33  
 Kewley, L. J., Dopita, M. A., Leitherer, C., et al. 2013, *ApJ*, 774, 100  
 Kewley, L. J., Nicholls, D. C., & Sutherland, R. S. 2019, *ARA&A*, 57, 511  
 Kriek, M., Shapley, A. E., Reddy, N. A., et al. 2015, *ApJS*, 218, 15  
 Kriek, M., van Dokkum, P. G., Labbé, I., et al. 2009, *ApJ*, 700, 221  
 Osterbrock, D. E., & Ferland, G. J. 2006, *Astrophysics of Gaseous Nebulae and Active Galactic Nuclei* (Sausalito, CA: University Science Books)  
 Reddy, N. A., Kriek, M., Shapley, A. E., et al. 2015, *ApJ*, 806, 259  
 Sánchez, S. F., Avila-Reese, V., Hernandez-Toledo, H., et al. 2018, *RMxAA*, 54, 217  
 Sánchez, S. F., Pérez, E., Sánchez-Blázquez, P., et al. 2016, *RMxAA*, 52, 171  
 Sanders, R. L., Shapley, A. E., Reddy, N. A., et al. 2020, *MNRAS*, 491, 1427  
 Sanders, R. L., Shapley, A. E., Zhang, K., & Yan, R. 2016, *ApJ*, 816, 23  
 Sanders, R. L., Shapley, A. E., Zhang, K., & Yan, R. 2017, *ApJ*, 850, 136  
 Sanders, R. L., Shapley, A. E., Zhang, K., & Yan, R. 2018, *ApJ*, 858, 99  
 Shapley, A. E., Sanders, R. L., Shao, P., et al. 2019, *ApJL*, 881, L35  
 Stanway, E. R., & Eldridge, J. J. 2018, *MNRAS*, 479, 75  
 Steidel, C. C., Rudie, G. C., Strom, A. L., et al. 2014, *ApJ*, 795, 165  
 Steidel, C. C., Strom, A. L., Pettini, M., et al. 2016, *ApJ*, 826, 159  
 Strom, A. L., Steidel, C. C., Rudie, G. C., et al. 2017, *ApJ*, 836, 164  
 Strom, A. L., Steidel, C. C., Rudie, G. C., Trainor, R. F., & Pettini, M. 2018, *ApJ*, 868, 117  
 Tayal, S. S., Zatsarinny, O., & Sossah, A. M. 2019, *ApJS*, 242, 9  
 Tremonti, C. A., Heckman, T. M., Kauffmann, G., et al. 2004, *ApJ*, 613, 898  
 Veilleux, S., & Osterbrock, D. E. 1987, *ApJS*, 63, 295  
 York, D. G., Adelman, J., Anderson, J. E., Jr., et al. 2000, *AJ*, 120, 1579  
 Zahid, H. J., Kashino, D., Silverman, J. D., et al. 2014, *ApJ*, 792, 75  
 Zhang, K., Yan, R., Bundy, K., et al. 2017, *MNRAS*, 466, 3217